The giant lobes of Centaurus A observed at 118 MHz with the Murchison Widefield Array

B. McKinley,[1,2]⋆ F. Briggs,[1,2] B. M. Gaensler,[2,3] I. J. Feain,[4] G. Bernardi,[5,6]
R. B. Wayth,[2,7] M. Johnston-Hollitt,[8] A. R. Offringa,[1,2] W. Arcus,[7] D. G. Barnes,[9]
J. D. Bowman,[10] J. D. Bunton,[4] R. J. Cappallo,[11] B. E. Corey,[11] A. A. Deshpande,[12]
L. deSouza,[3,4] D. Emrich,[7] R. Goeke,[13] L. J. Greenhill,[5] B. J. Hazelton,[14] D. Herne,[7]
J. N. Hewitt,[13] D. L. Kaplan,[15] J. C. Kasper,[5] B. B. Kincaid,[11] R. Koenig,[4]
E. Kratzenberg,[11] C. J. Lonsdale,[11] M. J. Lynch,[7] S. R. McWhirter,[11]
D. A. Mitchell,[2,16] M. F. Morales,[14] E. Morgan,[13] D. Oberoi,[17] S. M. Ord,[2,7]
J. Pathikulangara,[4] T. Prabu,[12] R. A. Remillard,[13] A. E. E. Rogers,[11] D. A. Roshi,[18]†
J. E. Salah,[11] R. J. Sault,[16] N. Udaya Shankar,[12] K. S. Srivani,[12] J. Stevens,[4,19]
R. Subrahmanyan,[2,12] S. J. Tingay,[2,7] M. Waterson,[1,7] R. L. Webster,[2,16]
A. R. Whitney,[11] A. Williams,[7] C. L. Williams[13] and J. S. B. Wyithe[2,16]

[1]*Research School of Astronomy and Astrophysics, Australian National University, Canberra, ACT 2611, Australia*
[2]*ARC Centre of Excellence for All-sky Astrophysics (CAASTRO), Australian National University, Canberra, ACT 2611, Australia*
[3]*Sydney Institute for Astronomy, School of Physics, The University of Sydney, NSW 2006, Australia*
[4]*CSIRO Astronomy and Space Science, Marsfield NSW 2122, Australia*
[5]*Harvard–Smithsonian Center for Astrophysics, Cambridge, MA 02138, USA*
[6]*Square Kilometre Array South Africa (SKA SA), Cape Town 7405, South Africa*
[7]*International Centre for Radio Astronomy Research, Curtin University, Bentley WA 6102, Australia*
[8]*School of Chemical & Physical Sciences, Victoria University of Wellington, Wellington 6140, New Zealand*
[9]*Monash e-Research Centre, Monash University, Clayton VIC 3168, Australia*
[10]*School of Earth and Space Exploration, Arizona State University, Tempe, AZ 85287, USA*
[11]*MIT Haystack Observatory, Westford, MA 01886, USA*
[12]*Raman Research Institute, Bangalore 560080, India*
[13]*Kavli Institute for Astrophysics and Space Research, Massachusetts Institute of Technology, Cambridge, MA 02139, USA*
[14]*Department of Physics, University of Washington, Seattle, WA 98195, USA*
[15]*Department of Physics, University of Wisconsin–Milwaukee, Milwaukee, WI 53201, USA*
[16]*School of Physics, The University of Melbourne, Parkville VIC 3010, Australia*
[17]*National Centre for Radio Astrophysics, Tata Institute for Fundamental Research, Pune 411007, India*
[18]*National Radio Astronomy Observatory, Charlottesville and Green Bank, USA*
[19]*School of Mathematics and Physics, University of Tasmania, Hobart, TAS 7001, Australia*

ABSTRACT

We present new wide-field observations of Centaurus A (Cen A) and the surrounding region at 118 MHz with the Murchison Widefield Array (MWA) 32-tile prototype, with which we investigate the spectral-index distribution of Cen A's giant radio lobes. We compare our images to 1.4 GHz maps of Cen A and compute spectral indices using temperature–temperature plots and spectral tomography. We find that the morphologies at 118 MHz and 1.4 GHz match very closely apart from an extra peak in the southern lobe at 118 MHz, which provides tentative evidence for the existence of a southern counterpart to the northern middle lobe of Cen A. Our spatially averaged spectral indices for both the northern and southern lobes are consistent with

⋆ E-mail: ben@mso.anu.edu.au

previous analyses, however we find significant spatial variation of the spectra across the extent of each lobe. Both the spectral-index distribution and the morphology at low radio frequencies support a scenario of multiple outbursts of activity from the central engine. Our results are consistent with inverse-Compton modelling of radio and gamma-ray data that support a value for the lobe age of between 10 and 80 Myr.

1 INTRODUCTION

Radio galaxies consist of two or more extended regions of magnetized plasma and synchrotron-emitting, relativistic charged particles, emanating from the active galactic nucleus (AGN) of a host galaxy (Begelman, Blandford & Rees 1984). These radio lobes interact with the intergalactic medium and/or intracluster medium and grow in size over time, due to either a quasi-continuous injection of particles from the jets or possibly separate episodic outbursts (Subrahmanyan, Saripalli & Hunstead 1996; Morganti et al. 1999). At GHz frequencies, the emission spectra of radio galaxies, within the observing band of a typical radio telescope, are often well described by a simple power law of the form $S \propto \nu^{\alpha}$, as a function of frequency, ν, where S is the observed flux density and α is the spectral index. The power-law spectrum results from the power-law energy distribution of relativistic particles producing the observed synchrotron emission. Inverse Compton emission may also be observed in radio galaxies when relativistic particles upscatter low-energy background photons, the most abundant of which are from the cosmic microwave background, to higher energies. Combining X-ray and gamma-ray data with radio data can therefore be used to constrain models of synchrotron and inverse Compton emission to estimate the physical properties of radio galaxies.

One of the most well-known and well-studied radio galaxies is Centaurus A (Cen A). This Fanaroff & Riley class I (FRI; Fanaroff & Riley 1974) radio source associated with the elliptical galaxy NGC 5128 was first discovered by Bolton (1948) at 100 MHz, the frequency we return to here in this paper. Cen A lies at a distance of a mere 3.8 ± 0.1 Mpc (Harris, Rejkuba & Harris 2010), making it the closest radio galaxy by a large margin and providing an ideal laboratory for studying the properties and particle acceleration histories of radio galaxies. Cen A has been studied intensely over a wide range of wavelengths and physical scales (see Israel 1998 for a review), but there is still much to be learned from this complex, nearby object.

The giant lobes of Cen A have a distinctive morphology with multiple peaks and orientations that change with distance from the core. They comprise a pair of inner lobes emanating from the core of the galaxy with a combined extent of $\sim$11 kpc, aligned at a position angle of 55° anti-clockwise from the north–south axis (Schreier, Burns & Feigelson 1981; Clarke, Burns & Norman 1992). Further from the core, the northern inner lobe is followed by a 'northern middle lobe' (NML; Morganti et al. 1999), which is the brightest part of the northern lobe situated $\sim$30 kpc from the core and orientated at a position angle of 45°. No southern counterpart to the NML has so far been detected in total intensity measurements (Feain et al. 2011), but O'Sullivan et al. (2013) have reported the existence of a region of high fractional polarization in the southern lobe that could be the oppositely directed counterpart to the NML. Finally, there are the giant outer lobes, which have a combined extent of $\sim$500 kpc. The northern outer lobe has a position angle of between 0° and 20° closest to the core, and then has an abrupt change in position angle at approximately RA (J2000) $13^{\text{h}}25^{\text{m}}00^{\text{s}}$,

Dec (J2000) $-40°58'00''$ (Cooper et al. 1965; Haynes, Cannon & Ekers 1983; Feain et al. 2011). The southern outer lobe also experiences a change in position angle, but one that is more gradual.

To produce the complex structure of Cen A, current models invoke a combination of separate, multiple outbursts of nuclear activity (Morganti et al. 1999), combined with interaction with the ambient medium (Burns 1986; Norman, Burns & Sulkanen 1988) and a precessing central engine (Haynes et al. 1983). An alternative explanation is that the jets interact with rotating gaseous shells (identified in optical observations by Malin, Quinn & Graham 1983, in 21 cm emission by Schiminovich et al. 1994, and in the far-infrared by Stickel et al. 2004) surrounding the host galaxy (Gopal-Krishna & Saripalli 1984; Gopal-Krishna & Wiita 2010). Further observational and theoretical work is required to determine the origins and evolutionary history of the giant lobes.

A new generation of low-frequency radio interferometers is beginning to produce scientific results and can provide more information on the shape of the radio spectrum of radio galaxies such as Cen A with reasonable angular resolution. These instruments, including the Low Frequency Array (LOFAR; van Haarlem et al. 2013), the Precision Array for Probing the Epoch of Reionization (PAPER; Parsons et al. 2010) and the Murchison Widefield Array (MWA; Lonsdale et al. 2009; Bowman et al. 2013; Tingay et al. 2013), aim to detect the faint redshifted 21-cm spectral line signal from the epoch of reionization (EoR). They have been designed to have the wide fields of view and short baselines required to detect the EoR signal, which is expected to have characteristic angular scales up to tens of arcmin (Furlanetto et al. 2006; Morales & Wyithe 2010; Pritchard & Loeb 2012), as well as the longer baselines that provide the angular resolution required for accurate instrument calibration. Therefore, these types of instruments are also ideally suited to measuring the low-frequency properties of extended objects such as Cen A.

In this paper we present a spatially resolved radio-frequency spectral-index study of the giant lobes of Cen A using data from the MWA 32 Tile prototype (MWA 32T) at 118 MHz and Parkes data at 1.4 GHz (O'Sullivan et al. 2013). In Section 2, we discuss previous radio observations and spectral analyses of the giant lobes. In Section 3, we provide the details of the MWA observations and data reduction. In Section 4, we present the results of the MWA observations and our analysis of the spatial and spectral properties of the giant lobes between 118 MHz and 1.4 GHz. In Section 5, we discuss the results in relation to current models of the origin and evolution of the giant lobes.

2 PREVIOUS OBSERVATIONS AND ANALYSES OF THE GIANT LOBES

Cen A has a large angular extent of $4° \times 8°$, making observations of the *entire* radio source difficult, especially when attempting to obtain images with reasonable angular resolution. Studies of the entire source at radio frequencies include full polarization maps obtained by Cooper et al. (1965) at 406, 960, 1410, 2650 and 5000 MHz

using the Parkes Radio Telescope (with resolutions ranging from 48 to 4 arcmin depending on frequency) and polarization and total intensity maps of the full source at 4.75 GHz and 4-arcmin resolution produced by Junkes et al. (1993). More recently, Feain et al. (2011) have mapped the radio continuum structure of Cen A at 1.4 GHz at high angular resolution and O'Sullivan et al. (2013) have produced a more detailed Faraday rotation analysis.

Low-frequency observations of the giant lobes of Cen A have, until recently, suffered from poor angular resolution, e.g. the 408 MHz, 0°.85 resolution map of Haslam et al. (1982) and the 45 MHz, 4°.6 resolution map of Alvarez et al. (1997). Low-frequency (below 100 MHz), low angular resolution studies of the Cen A giant lobes have also been conducted by Hamilton & Haynes (1968), Ellis & Hamilton (1966), Shain (1959) and Sheridan (1958). A recent paper from the PAPER collaboration (Stefan et al. 2013) mapped Cen A and the surrounding field at 148 MHz with 20-arcmin resolution and constructed a spectral-index map using the frequency variation within their 100 MHz observing band; they claim to find evidence of spectral flattening in turbulent regions of the lobes identified by Feain et al. (2011). Their spectral-index analysis is only qualitative, however, due to large uncertainties in their total flux measurements, resulting in physically unrealistic spectral-index values of between 0 and −3 (see Stefan et al. 2013, fig. 4).

2.1 Previous spectral analyses

The only spatially resolved spectral-index maps of the giant lobes of Cen A in the literature are by Combi & Romero (1997) and more recently by Stefan et al. (2013). The Combi & Romero (1997) map utilizes single-dish data from Parkes at 408 MHz and 1.4 GHz and finds the spectral index to steepen at the edges of the northern lobe and to steepen with distance from the core in the southern lobe. However, when this spectral-index map is compared with the Cooper et al. (1965) map of total intensity at 406 MHz, there is a correlation in the southern lobe between areas of steep spectral index and the estimated foreground component of emission from the 'spur' feature of Galactic emission to the south-east (Cooper et al. 1965). The spectral steepening in the northern lobe appears to correlate with regions of lower total intensity (and hence lower signal-to-noise ratio against the Galactic foreground). Stefan et al. (2013) attempt to map the spectral-index distribution of the giant lobes within the PAPER bandwidth and claim that the spectral index between 130 and 165 MHz varies as a function of distance from the core, steepening initially and then flattening towards the outer regions of the giant lobes. However, there appears to be a correlation between the total intensity and spectral-index maps in this case, indicating a possible systematic error in the calculation related to signal-to-noise ratio. The error in the spectral-index maps is likely to be high in regions of low total intensity of the lobes where the bright Galactic foreground emission at low frequencies (de Oliveira-Costa et al. 2008; Bernardi et al. 2009) is a significant fraction of the emission, and particularly in the case of Stefan et al. (2013) where the fractional frequency over which the spectral index is computed is very small.

All other spectral-index calculations have been performed by taking ratios of flux densities summed over large regions, for example Alvarez et al. (2000) and Hardcastle et al. (2009). This type of calculation is prone to error due to the inclusion of flux from foreground and background sources and constant offsets in maps due to missing short spacings. This is reflected in the large errors included in the spectral-index estimates of Alvarez et al. (2000). The most detailed spectral-index measurements of the giant lobes to date are

from Hardcastle et al. (2009), who split the lobes into five large regions and use a combination of single-dish and 5-year Wilkinson Microwave Anisotropy Probe (WMAP) data (Hinshaw et al. 2009) to constrain models of the spectral energy distribution (SED) and to make predictions as to whether the *Fermi* Large Area Telescope (*Fermi*-LAT; Atwood et al. 2009) would detect gamma-ray emission from the lobes. Subsequent results from *Fermi*-LAT revealed strong gamma-ray detections in both the northern and southern lobes of Cen A (Abdo et al. 2010; Yang et al. 2012).

3 OBSERVATIONS AND DATA REDUCTION

The MWA 32T was a scaled-down prototype version of the MWA, consisting of 32 antenna tiles, each tile consisting of 16 crossed-dipole antennas above a conducting mesh ground plane. The prototype was operated over the period 2007 September to 2011 September within the radio-quiet Murchison Radio Observatory in Western Australia at a latitude of −26°.7. Cen A was observed with the MWA 32T over three consecutive nights from 2011 April 29 to 2011 May 1, using 80-s snapshot observations scheduled over a wide range of hour angles. Each snapshot observation used a different, fixed setting of the analogue beamformers. The observations used in this paper consisted of a 30.72 MHz frequency band covering the frequency range of 108 to 139 MHz. The resulting data set contained 80 snapshot observations, centred on 124 MHz, but only the lower 20 MHz was used in imaging for reasons that will be discussed below. These snapshot observations were converted to UVFITS format and imported into CASA (Common Astronomy Software Applications) at a resolution of 1 s in time and 40 kHz in frequency. CASA was used for all further data reduction. AOFLAGGER (Offringa et al. 2010, 2012) was used to flag radio frequency interference (RFI) in each individual CASA measurement set. Additionally the central 40-kHz fine channel in each 1.24-MHz 'coarse channel' and three fine channels at each coarse channel edge were flagged due to known rounding errors and aliasing, respectively. The measurement sets were then averaged to 4-s and 160-kHz resolution and concatenated into a single CASA measurement set.

We performed self-calibration on Cen A itself, beginning with a simple, flat-spectrum point source model at the phase centre, while excluding baselines shorter than 100 λ. This was an effective calibration strategy, since the longer baselines do not resolve the bright central core of Cen A, while excluding the shorter baselines removes the effect of the diffuse emission. A multi-frequency synthesis image of the entire 30.72 MHz bandwidth was made using a relatively shallow CLEAN in CASA in order to improve the sky model, and a single self-calibration iteration was then performed across this frequency band. The final image used a 20-MHz sub-band at a centre frequency of 118 MHz in order to have the widest (and simplest) primary beam shape. Use of only the lower 20 MHz of the bandwidth was found to reduce imaging artefacts around the centre of the source. It was found that natural weighting and simple Cotton–Schwab CLEAN, without using the multiscale option, produced the best images. The W-projection algorithm (Cornwell, Golap & Bhatnagar 2008) was used to account for widefield effects.

The imaging did not take into account the changing primary beam shape that varies as a function of frequency and time, making the beam and its polarization properties different for each beamformer setting. This could be addressed using a Mosaic CLEAN if MWA primary beam shape images could be supplied to CLEAN. However, this functionality is currently not available and would require further development to be included in CASA. Our approach differs from that of Williams et al. (2012), who combined snapshots in the image
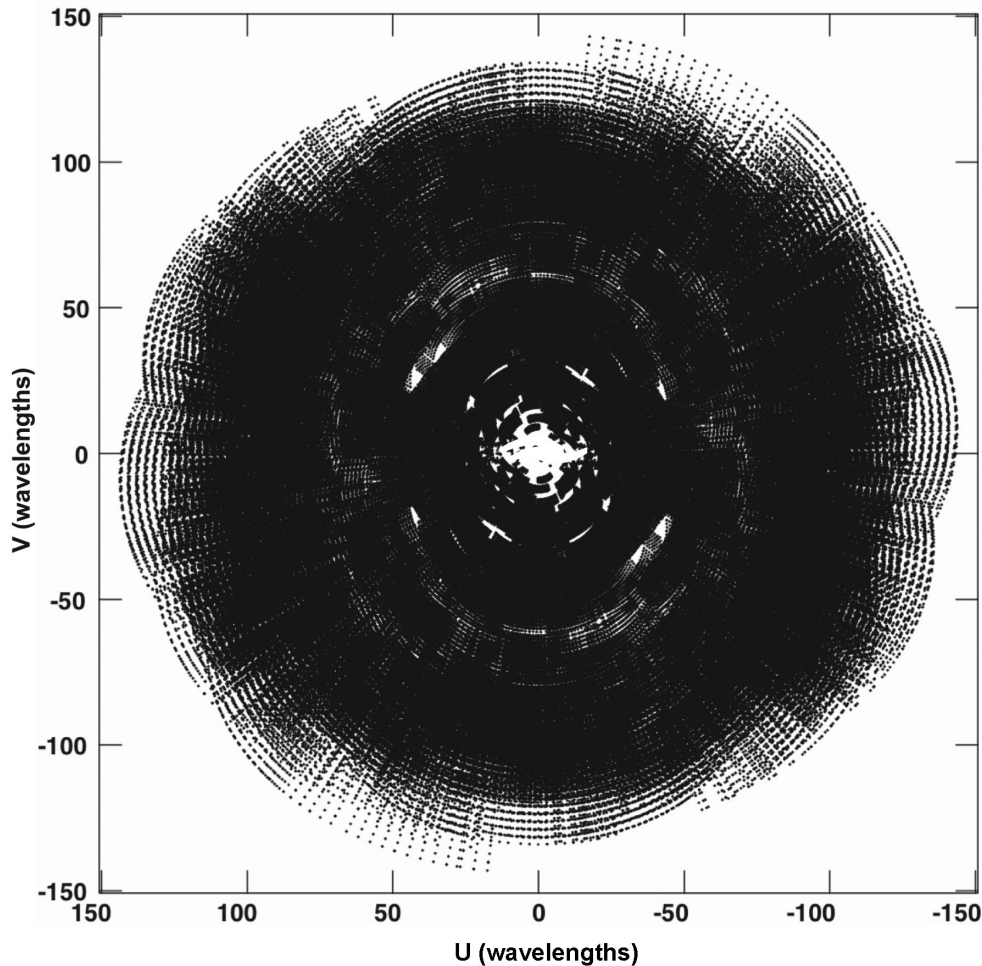
Figure 1. Combined uv-coverage for all snapshots centred on 118 MHz with a bandwidth of 20 MHz, in units of wavelength. The plot does not include the three shortest baselines, which were excluded from calibration and imaging.

domain, allowing them to assume a constant primary beam shape over each snapshot. The difference in approach is due to the scientific goal of imaging the large-scale structure associated with Cen A and the foreground Milky Way with a very small number of short baselines. Earth rotation synthesis was required in order to increase the uv-coverage of the short spacings and to allow the CLEAN algorithm to reconstruct the large-scale structure. The combined uv-coverage for all snapshots at a centre frequency of 118 MHz, with a bandwidth of 20 MHz, is shown in Fig. 1.

The MWA tile beam shape is different for both instrumental polarizations and varies as a function of frequency and time (due to different beamformer settings). An average 'Stokes I' primary beam image was calculated by summing analytic primary beams calculated for each instrumental polarization at each beamformer setting, using the same analytic primary beam model as Williams et al. (2012), and then taking the average of the two instrumental polarization beamshapes. The average primary beam for the 118-MHz image is shown in Fig. 2. The peak of the average primary beam in Fig. 2 is approximately $2°$ north of the core of Cen A, due to the discrete nature of the beamformer settings used to electronically point the telescope tiles. The average primary beam correction was applied in image space to the final cleaned image. This approach assumes that each tile beam is the same, when in fact there will be some variation in the beam shapes between tiles.

Bernardi et al. (2013) have shown that the error introduced by the tile beam model used in MWA 32T observations at 189 MHz, also assuming the same beam shape for each tile, is at about the 2 per cent level.

Since self-calibration on Cen A did not provide us with an overall flux scale, the flux scale was set using an ensemble of point sources within the full-width half-maximum (FWHM) of the primary beam. The Culgoora catalogue (Slee 1977, 1995) is the only point source catalogue covering this region of sky at the frequencies of interest. Eight unresolved Culgoora sources with measurements at both 80 and 160 MHz were identified within a $10°$ radius of Cen A. A scaling factor was calculated for each of these sources by dividing its expected flux density (based on the Culgoora measurements at 80 and 160 MHz) by its measured flux density in the primary-beam-corrected MWA image. The details of the sources used to set the flux density scale in the MWA map at 118 MHz are given in Table 1. The scaling factors are large because the flux density of the core of Cen A was arbitrarily set to 1 Jy in the initial calibration. The standard deviation of the scaling factors listed in Table 1 is 319, which is 22 per cent of the average scaling factor of 1438. We therefore estimate the uncertainty in the flux scale of the MWA image of Cen A to be $±22$ per cent. This is similar to the result of Jacobs, Bowman & Aguirre (2013) who calculate a flux-scale uncertainty of 20 per cent for the MWA 32T over the full extent of its
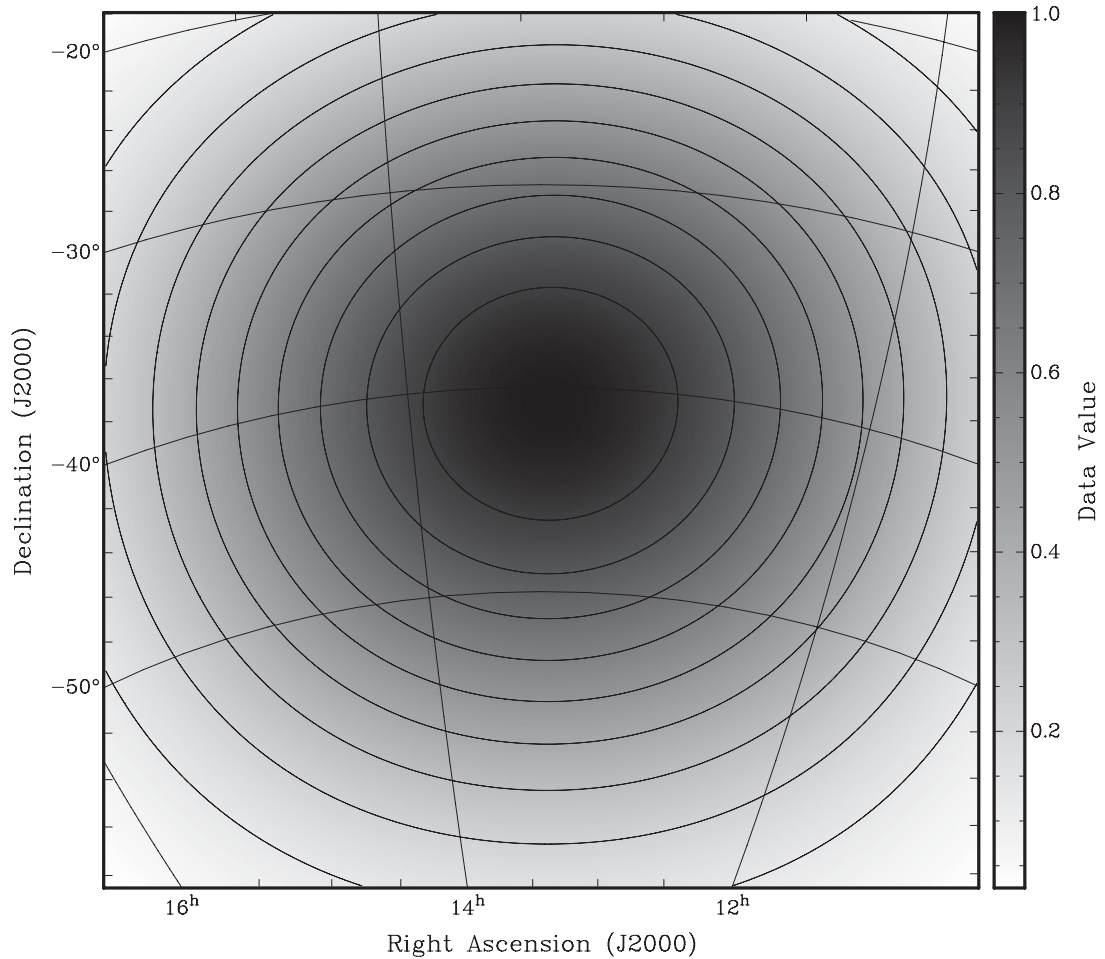
Figure 2. Average tile primary beam from an analytic model. The centre frequency is 118 MHz. Contours are from 10 to 90 per cent of the peak gain (normalized to 1), incrementing in steps of 10 per cent.

Table 1. Sources Used to Set Flux Density Scale.

Source name	Expected flux at 118 MHz (Jy)	Scaling factor
PKS B1346−391	23.2	1946
PKS B1246−410	31.6	1156
PKS B1247−401	15.4	1185
PKS B1340−373	6.6	1699
PKS B1355−416	32.1	1237
PKS B1243−412	13.7	1870
PKS B1233−416	12.7	1153
PKS B1407−425	13.4	1253
	Average Scaling Factor:	1438

~25° field of view and attribute most of this error to uncertainties in the primary beam model and to errors introduced by the CLEAN algorithm.

4 RESULTS AND ANALYSIS

Fig. 3 shows the MWA image of the Cen A field at 118 MHz with the primary beam correction and flux scale applied. At this frequency, the spatial resolution is approximately 25 arcmin. The uv-range for this image was restricted to exclude the shortest three baselines of the MWA 32T that are problematic for calibration and imaging. This also effectively filters out features on scales larger than about 12°, which would include much of the large-scale Galactic emission expected at these frequencies. Due to the similarities between PAPER and the MWA, many of the same imaging and calibration challenges described by Stefan et al. (2013) have also been encountered in this work. We note that the missing short baselines in the MWA images result in a negative bowl around Cen A, which affects the measurement of flux densities to some extent. Fig. 4 shows a profile through the centre of the MWA image along a constant declination of (J2000) $-43°01'9''$. It appears from Fig. 4 that the negative bowl, on the order of a few Jy beam^{-1}, is roughly constant within a 5° radius of the core of Cen A and hence has little effect on most of the subsequent analysis of Cen A's giant lobes. The total integrated flux density of the entire source in our 118 MHz image, measured by summing the flux in Cen A above the 2.5 Jy beam^{-1} contour level, is 6620 ± 1460 Jy. Alvarez et al. (2000) show that the flux-density spectrum integrated over the full extent of Cen A follows a power law with a spectral index of $-0.70 ± 0.01$ from 10 MHz to 4.75 GHz and their fig. 2 predicts a flux density of approximately 7250 Jy. Our measured flux density for the entire source is consistent with the predicted value of Alvarez et al. (2000).

The peak flux density of Cen A at 118 MHz is 1698 ± 374 Jy beam^{-1} (where the Gaussian restoring beam is
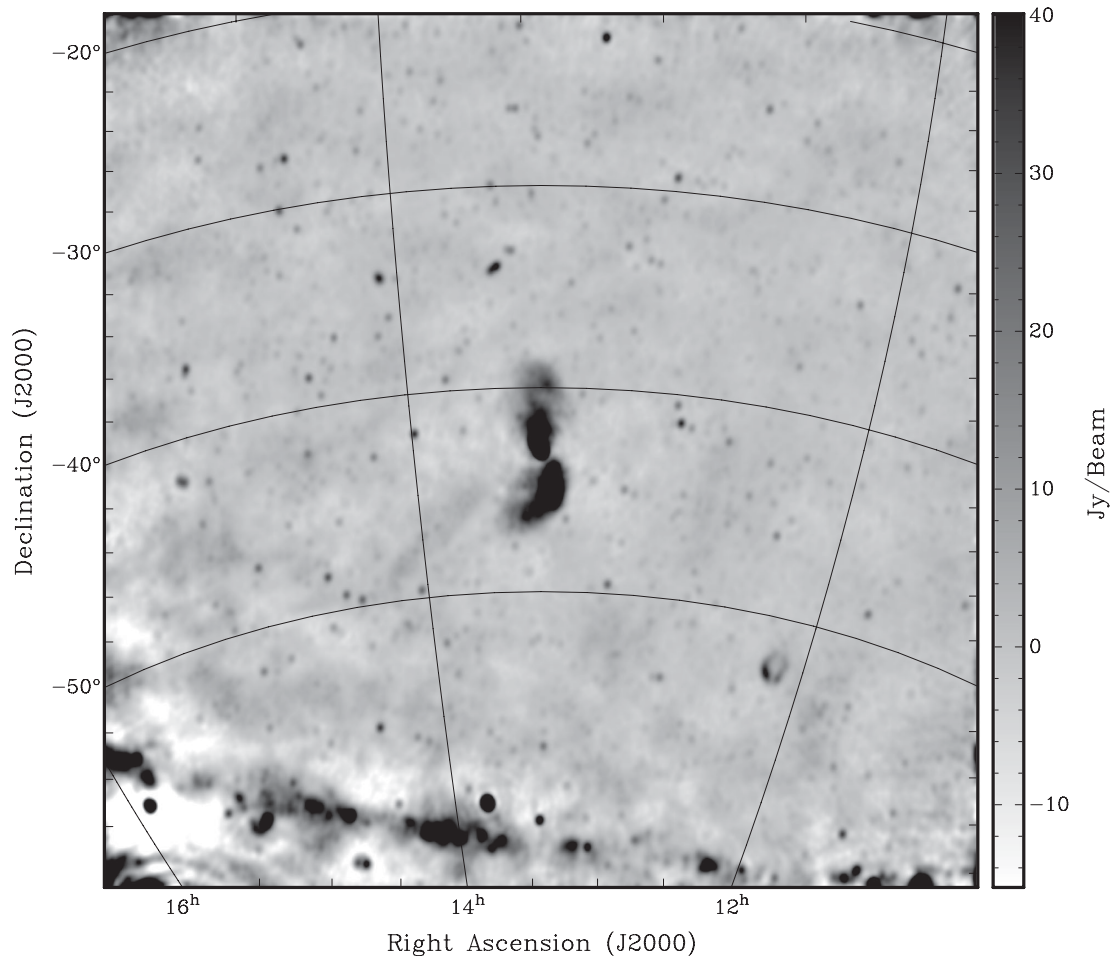
Figure 3. Cen A and surrounding field at 118 MHz with the MWA 32-Tile prototype. The image is shown on a linear scale between −15 and +40 Jy beam^{-1}. It has an angular resolution of 25 arcmin and an rms noise of approximately 0.5 Jy beam^{-1} in 'empty' regions of the map.

$0°38 \times 0°32$ with a major axis position angle of 171°) at RA (J2000) $13^h25^m28^s$, Dec (J2000) −43°01′9″. This position is consistent with the known position of the centre of the radio source given by Ma et al. (1998). At our angular resolution of 25 arcmin, the central resolution element contains the entirety of the inner lobes and the brightest part of the NML. The rms in a typical 'empty' region of the image is approximately 0.5 Jy beam^{-1}, giving a dynamic range of at least 3000. At this frequency, the primary beam FWHM is approximately 31°, and many faint point sources occupy the field of view. Apart from Cen A, other distinctive features visible in Fig. 3 include the supernova remnant G296.5+10.0 in the south-west and the Galactic plane along the bottom of the image. The Galactic plane is not well reconstructed by the MWA 32T due to its large angular size, which is not sampled by the shortest baselines. Additionally, the Galactic plane is well outside the FWHM of the tile primary beam. Despite the relatively small number of short baselines, faint diffuse emission from the Milky Way on scales smaller than 12° can be seen across the map. To show that these large-scale structures in the surrounding field are real and not imaging artefacts, we show in Fig. 5 a comparison between the 408 MHz map of Haslam et al. (1982) and the MWA 118 MHz map. The MWA image has been smoothed to the same resolution as the 408 MHz map (0°85). The original Haslam et al. (1982) data show a roughly linear decrease in average intensity from the south-east corner to the north-west

(presumably due to Galactic emission). This large-scale gradient, undetectable to the shortest baselines of the MWA 32T, has been subtracted away from the Haslam et al. (1982) map to make the smaller-scale structures clearer. In Fig. 5, much of the diffuse structure between the two images matches well by eye, particularly the shape of the giant radio lobes of Cen A themselves and the 'spur' feature to the south-east (label 1). Labels 2 and 3 in Fig. 5 show two other distinctive large-scale foreground features that appear in both maps. The qualitative comparison between the Haslam et al. (1982) and MWA maps confirms that the features on the angular scales associated with the Cen A giant lobes are being reconstructed properly in the MWA image. We do not pursue a spectral comparison with the Haslam map as the angular resolution is too coarse and the frequency difference between the two maps is too small for our purposes. Instead, we use data at 1.4 GHz for our spectral analysis.

Fig. 6 shows the MWA image at 118 MHz (in both grey-scale and contours) overlaid with the Parkes 1.4 GHz Stokes I contours from O'Sullivan et al. (2013). The 1.4 GHz map has been smoothed to the same resolution as the MWA map. The structure of Cen A at 118 MHz matches very closely with the structure seen at 1.4 GHz. However there are a few areas where the morphologies appear to be slightly different. Of particular interest is the northern part of the southern giant lobe at approximately RA (J2000) 13^h23^m, Dec. (J2000) −43°45′, where there appears to be additional structure
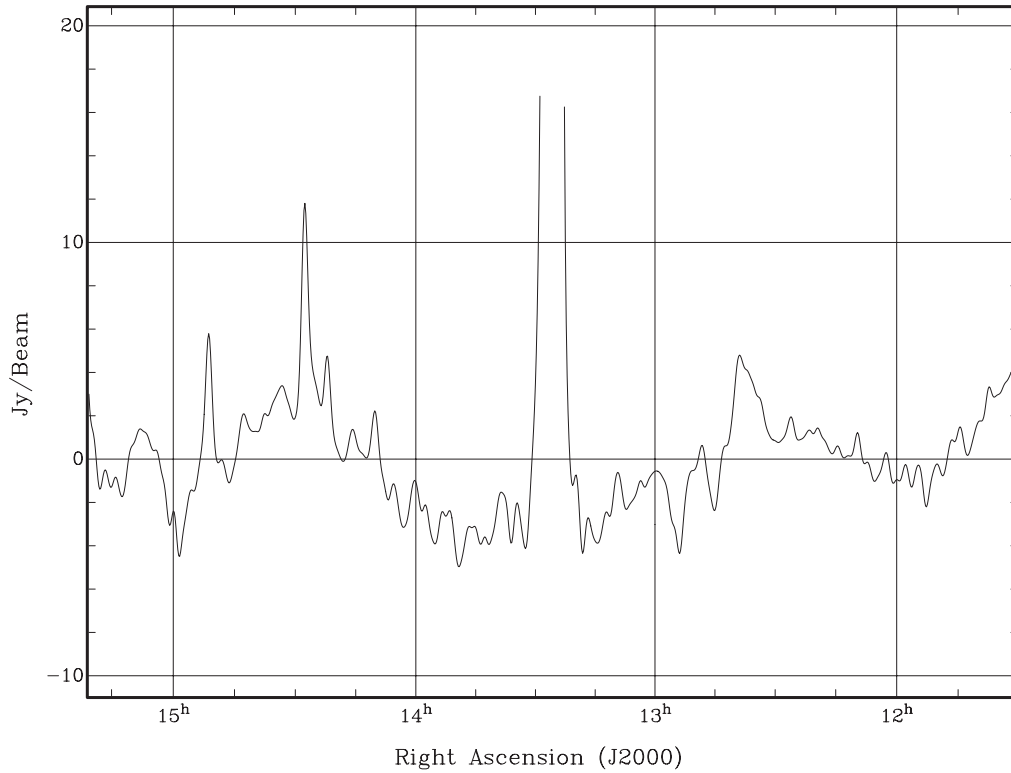
Figure 4. Profile through the centre of the MWA 118 MHz image of Cen A (see Fig. 3) along a constant declination of (J2000) $-43°01'9''$, showing the negative bowl surrounding the core of Cen A in the image.
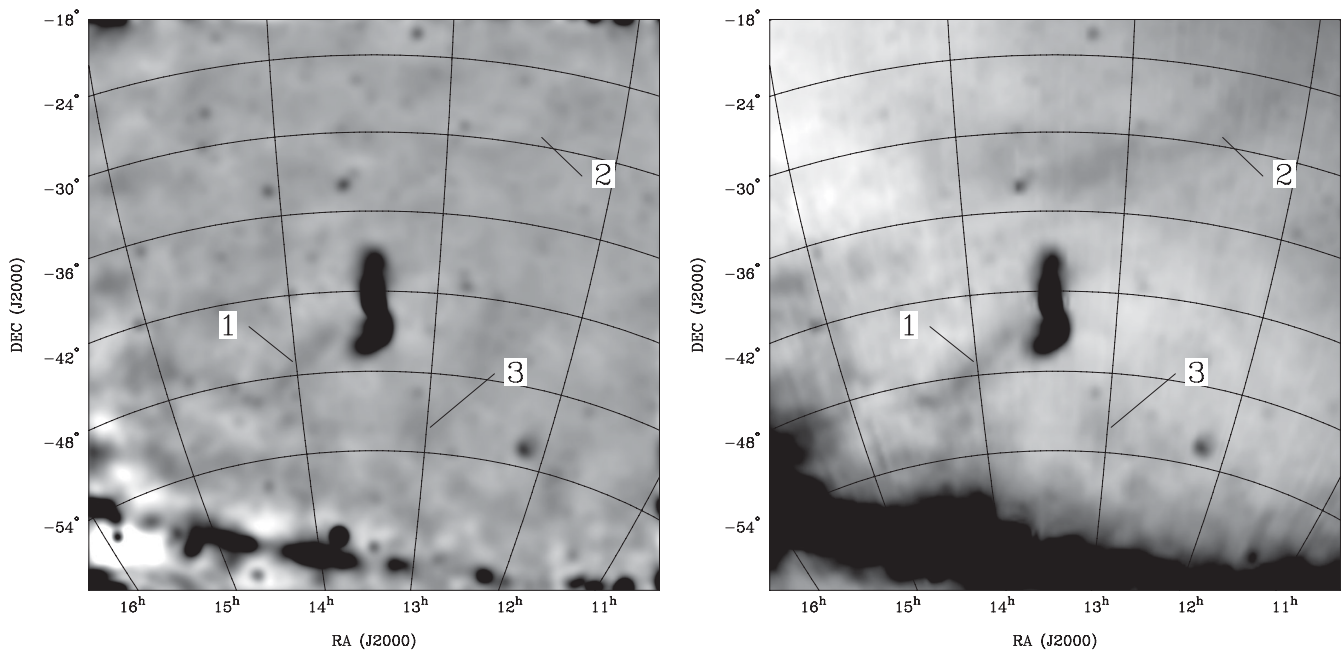

Figure 5. Comparison between the MWA 118 MHz image (left) and Haslam et al. (1982) 408 MHz image (right), both smoothed to the same angular resolution of $0°.85$. A linear brightness gradient has been subtracted from the Haslam et al. (1982) map to make the smaller-scale structures clearer. The faint diffuse structure on scales less than $12°$ matches well by eye. Labels 1 to 3 indicate large-scale foreground features clearly present in both maps.
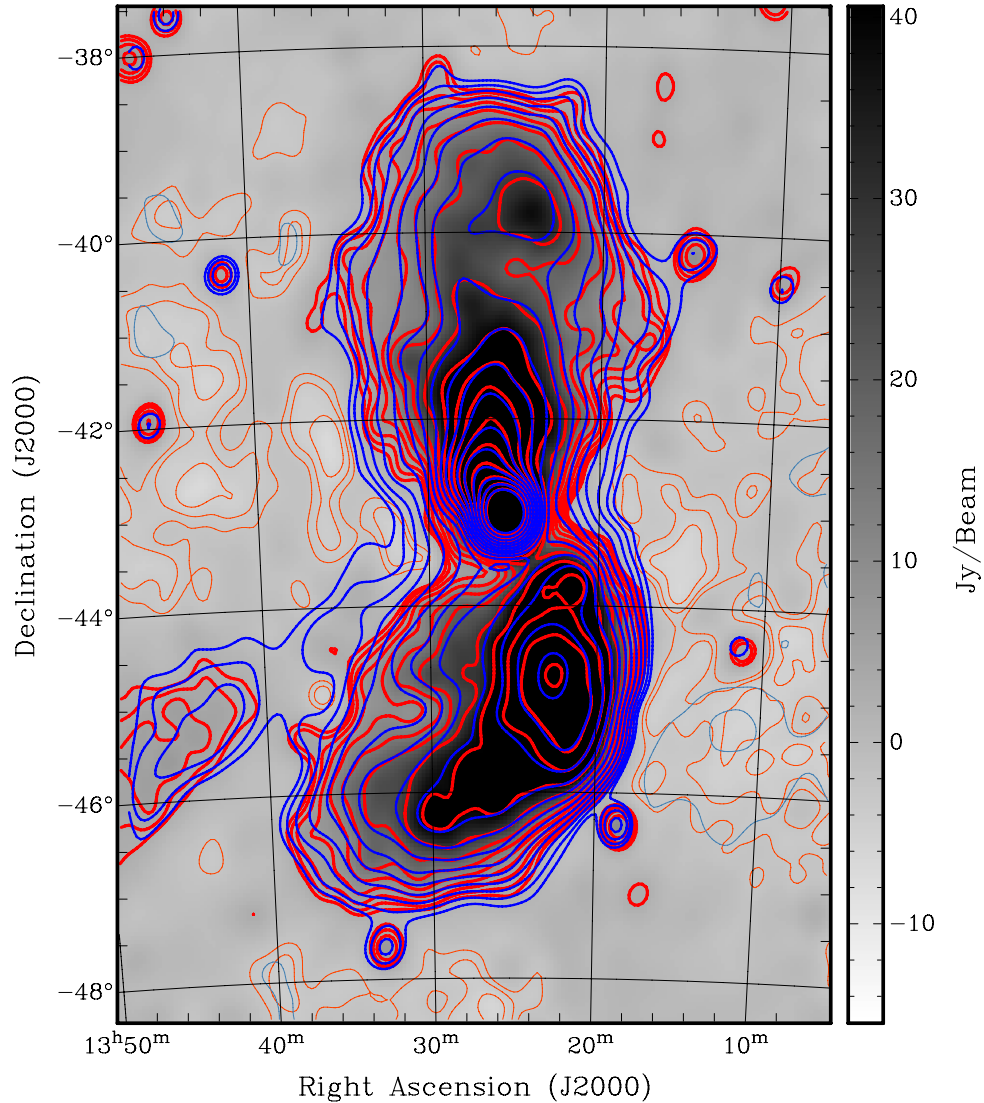
Figure 6. Cen A at 118 MHz (grey-scale and red contours) overlaid with Parkes 1.4 GHz contours in blue, smoothed to the same angular resolution of 25 arcmin. Positive contours are bold and start at 2.5 Jy beam^{-1} for 118 MHz and 0.50 Jy beam^{-1} for 1.4 GHz, incrementing in a geometric progression of $\sqrt{2}$. Negative contours (thinner and lighter shade) start at -2.5 Jy beam^{-1} for 118 MHz and -0.50 Jy beam^{-1} for 1.4 GHz and decrement in a geometric progression of $\sqrt{2}$.

at 118 MHz that is not present in the 1.4 GHz image. This is discussed further in combination with the spectral tomography results in Section 4.1.1.

4.1 Spectral index of the giant lobes

Calculation of the spectral index only within the 30 MHz MWA band is unlikely to produce accurate values since the fractional frequency coverage is too small to accurately measure changes in flux density. Instead, we compare data at 1.4 GHz (O'Sullivan et al. 2013) to our 118 MHz image in order to compute spectral indices. This larger frequency ratio makes the spectral-index calculations more robust to errors in both maps. The assumption of a single spectral index over such a large frequency range is simplistic as there could be curvature in the spectrum. However, between 118 MHz and 1.4 GHz the spectral curvature is expected to be small, as predicted by the inverse-Compton modelling of Yang et al. (2012); for example see their fig. 8.

We first measure the spectral indices of the giant lobes over the same regions as Hardcastle et al. (2009) using T-T plots. This technique accounts for the possibility of constant offsets between maps due to missing short spacings or large-scale foreground contamination. T-T plots were initially used in the analysis of astronomical observations to account for a constant but unknown component of antenna temperature being contributed by the ground in observations of the spectrum of Galactic radio emission (Turtle et al. 1962). The technique takes the brightness temperature of many points within a region of the sky (assumed to have the same spectral index) at two different frequencies and plots them against each other. If there is a constant offset between the brightness temperature values within a region due to emission from the ground (or any other reason) then this will be obvious in a T-T plot; the points in a T-T plot between frequencies ν_1 and ν_2 will fall along a line having a slope equal to $(\nu_1/\nu_2)^\alpha$, and with a non-zero y-intercept resulting from the constant offset between the two regions. At 118 MHz, the brightness temperature of the Galactic foreground is two orders of
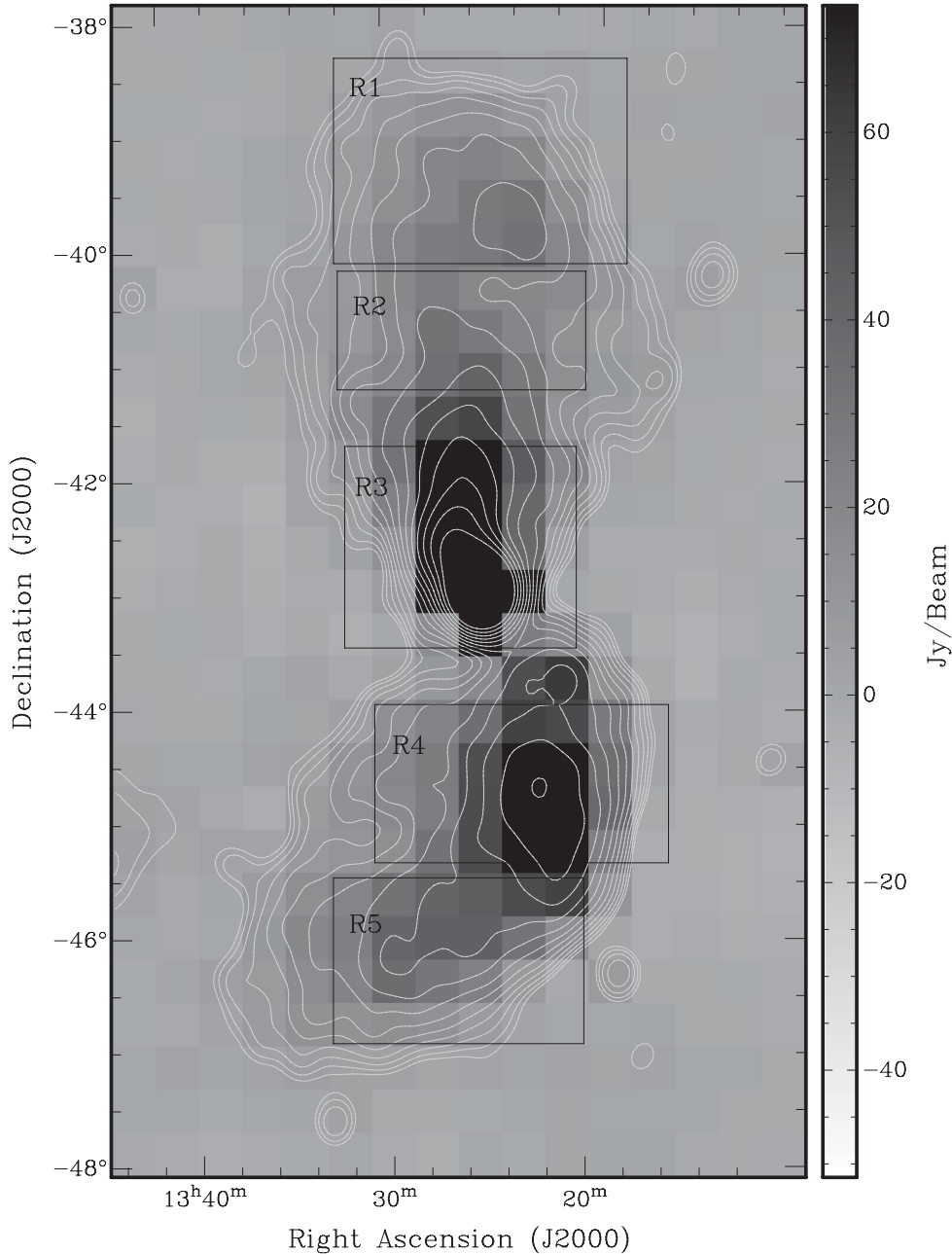
Figure 7. Regions from Hardcastle et al. (2009) used for constructing T-T plots, overlaid on the MWA 118 MHz image resampled to 1 pixel per beam. Contours are of the full resolution 118 MHz image, incrementing in a geometric progression of $\sqrt{2}$ from 2.5 Jy beam^{-1}.

magnitude higher than at 1.4 GHz and if significant on the spatial scales of our chosen regions, it would show up as a constant offset in T-T plots between 118 MHz and 1.4 GHz. The effects of missing flux due to missing short baselines in the interferometer data would also cause a constant offset in the T-T plots.

We constructed T-T plots for the five regions shown in Fig. 7, chosen to match with the regions defined by Hardcastle et al. (2009). Our region 3 differs from Hardcastle et al. (2009) in that we use a rectangle, rather than a circle, to define this region. The 1.4 GHz images were smoothed to the same 25-arcmin resolution as the MWA map (Fig. 3) and both images were resampled to make the pixel size as large as the synthesized beam. This produced independent measurements of the flux density at each (equally sized) pixel in

both images, allowing us to perform a chi-squared analysis. For each region, the flux densities at the low and the high frequencies at each pixel were plotted against each other. The error bars for each point were estimated by selecting off-source regions to the east and west of each of the regions in Fig. 7 and measuring the rms noise in each. These off-source regions were large enough to ensure that the rms measurement included both variations in Galactic foreground emission and the contribution of background point sources. The reduced chi-squared (χ^2_{red}) was also computed for each T-T plot and used as an indicator of the validity of the assumption of a single spectral index over the spatial extent of a given region. A line was fit to the data using orthogonal-distance regression (Boggs & Rogers 1990) and the spectral index for each region, α_R, was
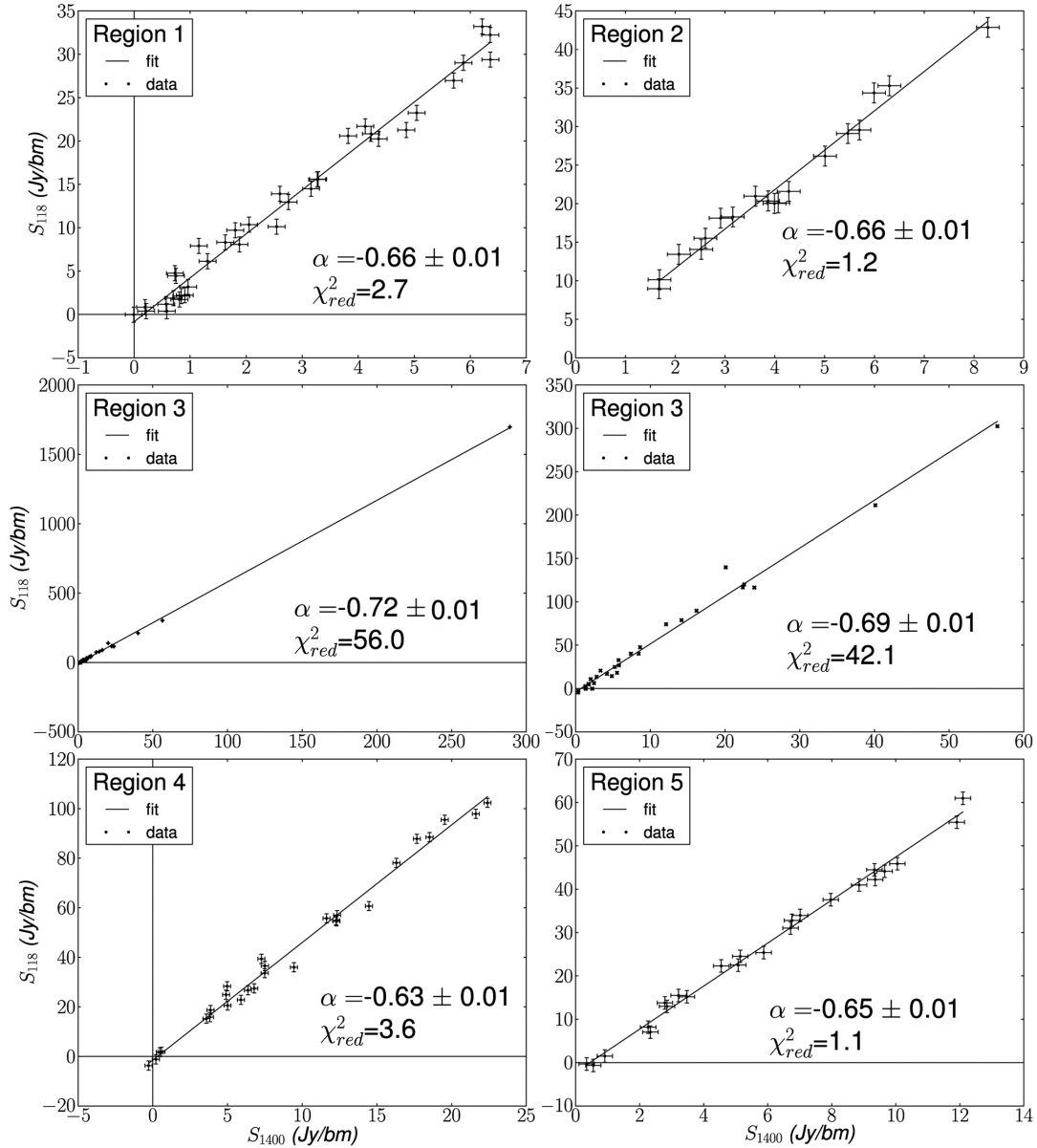
Figure 8. T-T plots for the five regions of the giant lobes of Cen A and the computed spectral indices between 118 and 1400 MHz, including the $\chi^2_{\rm red}$ values for each region as defined in Fig. 7. The centre row contains two plots for region 3; on the left all pixels have been included, and on the right the bright central pixel has been excluded to remove the influence of the inner lobes. The uncertainties in the spectral indices displayed are derived from the uncertainty in the slope of the line of best fit and represent random errors only. See text for the inclusion of systematic errors due to global flux scale uncertainties.

calculated using:

$$\alpha_R = \frac{\log(\Delta)}{\log(\nu_{\rm low}/\nu_{\rm high})}, \tag{1}$$

where Δ is the slope of the line of best fit for the T-T plot of region R and $\nu_{\rm low}$ and $\nu_{\rm high}$ are the low and high frequencies, respectively.

Fig. 8 shows T-T plots for the five regions of the giant lobes and the computed values of α and $\chi^2_{\rm red}$ for each. The centre row of Fig. 8 contains two plots for region 3; on the left all pixels have been included, and on the right the bright central pixel has been excluded to remove the influence of the inner lobes, since we are primarily concerned with the spectral indices of the giant outer lobes in this paper. The $\chi^2_{\rm red}$ values for regions 2 and 5, corresponding to the inner part of the northern outer lobe and the outer part of the southern outer lobe, respectively, are close to unity, indicating that

the spectral indices of these regions show little spatial variation. The T-T plots for region 3 have $\chi^2_{\rm red}$ values of 56.0, if the central pixel is included, and 42.1, if the central pixel is excluded. These $\chi^2_{\rm red}$ values are an order of magnitude larger than for the other regions, indicating significant spatial variation of the spectral index. This is probably due to the complex structure of the region that contains the NML. Regions 1 and 4 were also found to have high $\chi^2_{\rm red}$ values of 2.7 and 3.6, respectively. The variation in spectral index in these regions will be investigated in detail using spectral tomography in Section 4.1.1.

The spectral indices derived from the T-T plots can be considered as averages over each region and so can be compared to the values computed using summed flux densities in previous studies. The main source of error in the spectral indices is due to the 22 per cent uncertainty of the global flux scale in the MWA 118 MHz image.

This error does not affect differences in the spectral indices computed between regions. We therefore quote separately the systematic errors due to global flux scale uncertainties and the statistical errors due to random errors in the images. The error in the flux scale of the 1.4 GHz data is approximately 2 per cent (Baars et al. 1977; Reynolds 1994) and is negligible compared to the uncertainty at 118 MHz. We find a spectral index in regions 1 and 2 (northern outer lobe) of $\alpha_{1,2} = -0.66 \pm 0.01(\mathrm{stat})^{+0.10_{\mathrm{sys}}}_{-0.08_{\mathrm{sys}}}$, and in regions 4 and 5 (southern outer lobe) of $\alpha_4 = -0.63 \pm 0.01(\mathrm{stat})^{+0.10_{\mathrm{sys}}}_{-0.08_{\mathrm{sys}}}$ and $\alpha_5 = -0.65 \pm 0.01(\mathrm{stat})^{+0.10_{\mathrm{sys}}}_{-0.08_{\mathrm{sys}}}$, respectively. The calculated spectral-index values are consistent with Alvarez et al. (2000), who found the spectral indices of the northern and southern lobes between 408 MHz and 1.4 GHz to be -0.75 ± 0.08 and -0.70 ± 0.08, respectively. Our values are also consistent with the Hardcastle et al. (2009) spectral indices between 408 MHz and 1.4 GHz (which we calculated from the flux density values in their Table 1) of $\alpha_1 = -0.60 \pm 0.05$ and $\alpha_2 = -0.65 \pm 0.07$ in the northern lobe and $\alpha_4 = -0.47 \pm 0.06$ and $\alpha_5 = -0.62^{+0.12}_{-0.11}$ in the southern lobe.

As well as being averages across a given angular region, the spectral indices computed using T-T plots are averages along our line of sight. This presents a problem if there are overlapping regions with different spectral indices. In a scenario where the lobes were formed by multiple, separate outbursts from the central engine (Morganti et al. 1999; Saxton, Sutherland & Bicknell 2001), there could be overlapping structures of synchrotron-emitting particles produced during different epochs of activity, as discovered in another relatively close-by radio galaxy Hercules A (Gizani & Leahy 2003). In this case, the restarted jets forming the more recent lobe structures have a faster advance speed than the previous jets since they are travelling through an underdense region that has been cleared of material in the previous epoch of activity (Clarke & Burns 1991). As the new lobes catch up to the older lobes, this results in particles with different spectral ages (and presumably different spectral indices) overlapping along our line of sight. To investigate this possibility further we apply the technique of spectral tomography in Section 4.1.1.

4.1.1 Spectral tomography

The simple two-point spectral index generated by dividing images at different frequencies is unable to separate structures with different spectral indices when they are aligned along our line of sight, instead giving a weighted average of the two. Spectral tomography has been used to identify overlapping spectral structures within radio galaxies (Katz-Stone & Rudnick 1997; Gizani & Leahy 2003) and has also been applied to Galactic sources (DeLaney et al. 2002; Gaensler & Wallace 2003). Here we apply the technique to the giant lobes of Cen A to search for regions with distinctly different spectral indices, which may overlap along our line of sight and therefore may be difficult to detect using conventional methods.

Since the spectral index of each component is not known, a cube of images is generated, each with a different spectral component subtracted away. The cube of images, $M_{\mathrm{tom}}(\alpha_t)$, is given mathematically by

$$M_{\mathrm{tom}}(\alpha_t) \equiv M_{\mathrm{low}} - \left(\frac{\nu_{\mathrm{low}}}{\nu_{\mathrm{hi}}}\right)^{\alpha_t} M_{\mathrm{hi}}, \tag{2}$$

where M_{low} and M_{hi} are the low and high-frequency maps, ν_{low} and ν_{hi} are the low and high frequencies, respectively, and α_t is the trial spectral index for that image in the cube.

When the trial spectral index is correct, the component is subtracted perfectly and the region of the image appears to match with the background. Whenever the trial index is incorrect, the component is either under-subtracted or over-subtracted, making it appear lighter or darker than the background. The uncertainty in the spectral index is determined by the range of trial values in which a feature on the map is neither under-subtracted nor over-subtracted. The uncertainties quoted in this section are therefore due to random errors only and do not include the systematic error introduced by the uncertainty in the global flux scale. We generated a spectral tomography cube with trial spectral indices from -0.01 to -1.50, decrementing in steps of 0.01. When the tomography cube is viewed as a movie, it is clear that there are variations in spectral index with position across both the northern and southern outer lobes of Cen A. We show a subset of the images from the cube in Figs 9 and 10.

First we examine the northern lobe, and in particular region 1 where the χ^2_{red} of the T-T plot indicated that a power law with a single spectral index for the whole region was not a good model (see Fig. 8). A series of six slices of the tomography cube is shown in Fig. 9, with trial spectral indices from $\alpha_t = -0.45$ to $\alpha_t = -0.70$, decrementing in steps of 0.05. The spectral tomography reveals that the spatial distribution of spectral-index values is complex, and although the average value of around -0.65 (lower, centre panel) agrees well with the T-T plots, it is clear that there are a range of spectral-index values distributed across region 1 and across the rest of the northern lobe. In particular, the spectral index flattens significantly at a declination of around $-39°.5$ (label A) where the position angle of the northern lobe changes to form the outer northern-hook structure. From the tomography cube, we estimate that the spectral index of this flattened region is -0.55 ± 0.05 and steepens to -0.70 ± 0.05 at the end of the northern hook (label B). An interesting result is that a similar positional change in spectral index also occurs in the region closer to the core. Immediately south of declination $-42°$ there is a relatively flat region of spectral index -0.67 ± 0.01 (label D) which abruptly steepens to -0.72 ± 0.01 north of declination $-42°$ (label C). These features are most clearly seen where they are slightly over-subtracted or under-subtracted, hence the reason for showing slices at $\alpha_t = -0.65$ and $\alpha_t = -0.70$ in Fig. 9, rather than $\alpha_t = -0.67$ and $\alpha_t = -0.72$. There is also a distinctly steeper region at $13^h31^m18^s$, $-41°19'54''$; however this is not a feature of the lobes of Cen A. It is due to the background point source PKS 1328−410 (Large et al. 1981), which can also be seen clearly in the high-resolution map of Feain et al. (2011).

A subset of the spectral tomography cube zoomed in on the southern outer lobe is shown in Fig. 10. Although the large-scale morphology is quite different from the northern lobe, we do see similar changes in spectral index with position in the south. This is most prevalent in the northern region of the southern lobe (corresponding to region 4 in the T-T plots in Fig. 8). Of interest is the distinctly steeper region at approximately Dec. (J2000) $-43°45'$ (label E) with a spectral index of -0.69 ± 0.02 surrounded by regions of spectral index -0.57 ± 0.02 immediately to the north and south (label F). This is best seen in the lower-left panel ($\alpha_t = -0.59$) of Fig. 10, where the steeper feature is under subtracted, appearing darker than the flatter-spectrum region surrounding it. The feature labelled E in Fig. 10 appears to be present at 118 MHz but not at 1.4 GHz. To exclude the possibility that this could be due to a bright, steep-spectrum background point source, we have plotted in Fig. 11 the MWA and Parkes contours over the high-resolution ATCA+Parkes map of Feain et al. (2011). Fig. 11 shows that the additional peak at RA (J2000) 13^h23^m, Dec. (J2000) $-43°51'$ in
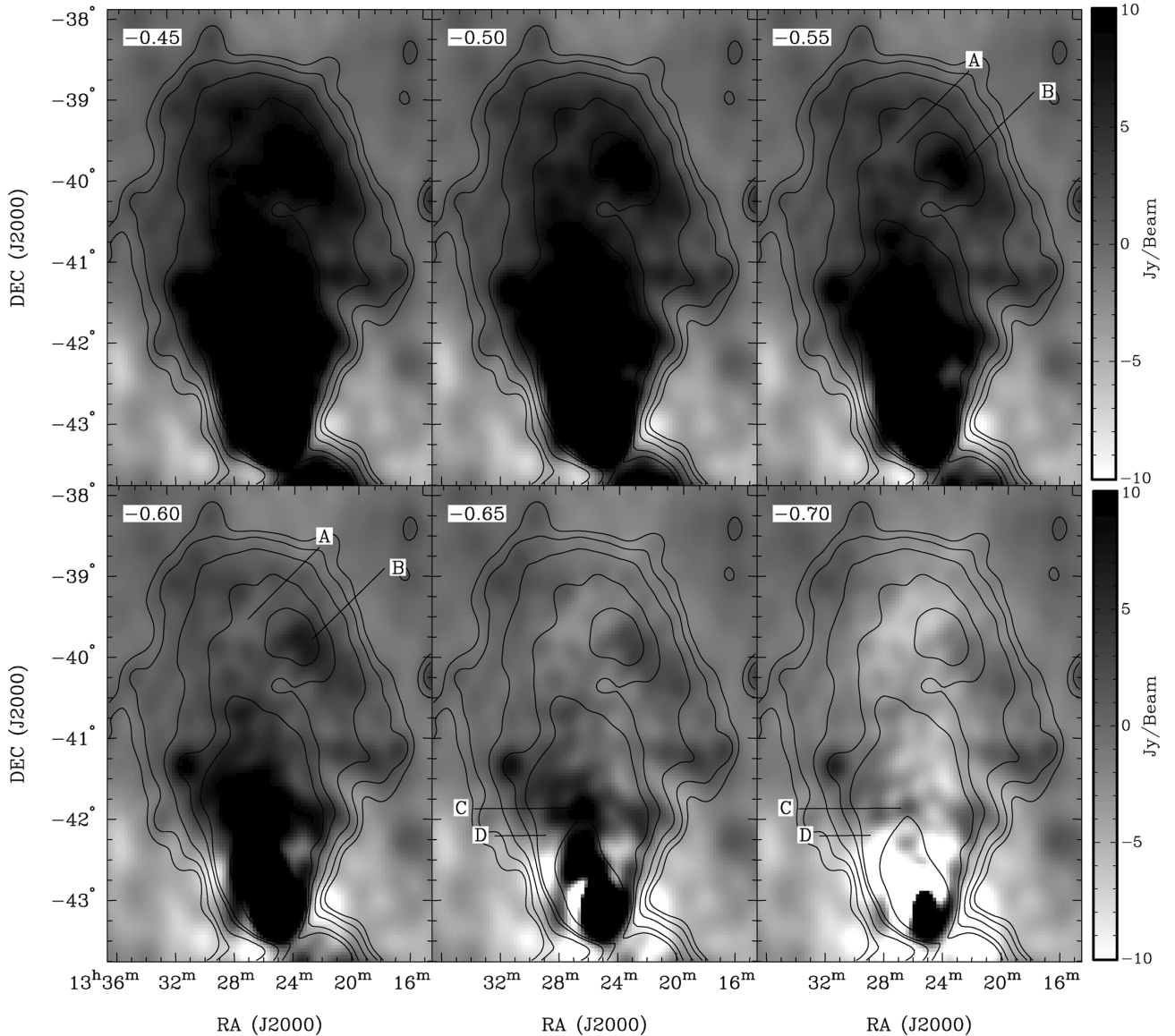
Figure 9. A subset of the spectral tomography images of the northern lobe between 118 MHz and 1.4 GHz with trial spectral indices as indicated in the top-left corner of each sub-image. Grey-scale is from -10 to 10 Jy beam^{-1}. Overlaid are contours from the 118 MHz image at 2.5, 5, 10, 20, 28.3 and 113 Jy beam^{-1}. The feature labelled A has a significantly flatter spectral index than that labelled B. Similarly, there is a change in spectral index between the flatter region labelled D and the steeper feature labelled C.

the 118 MHz map does not coincide with any background sources visible at 1.4 GHz. The bright extended source MRC 1318−434B (Schilizzi & McAdam 1975; Large et al. 1981) is clearly visible in the high-resolution grey-scale image and is largely responsible for the peak in the contours of the smoothed 118 MHz and 1.4 GHz images at RA (J2000) 13^{h}21^m, Dec. (J2000) $-43°48'$, which is approximately 30 arcmin away from the additional peak in the 118 MHz image. The positional registration of the two images is accurate to within 1 arcmin. Two other steep spectrum features that are prominent in Fig. 10 at RA (J2000) 13^{h}29^{m}38^s, Dec. (J2000) $-44°44'14''$ and RA (J2000) 13^{h}33^{m}57^s, Dec (J2000) $-46°41'32''$ are due to the background point sources SUMSS J132937−444413 (Mauch et al. 2003) and PMNM 133051.5-462614 (Large et al. 1981), respectively. Again, these bright background sources are clearly visible in the high-resolution map of Feain et al. (2011).

5 DISCUSSION

5.1 Morphology, spectral index and clues about lobe formation history

The morphology of Cen A at 118 MHz with 25-arcmin resolution matches closely with the single dish Parkes observations at 1.4 GHz, as shown in Fig. 6. The 15 arcmin gap between the northern and southern lobes reported by Feain et al. (2011) can also be seen in the 118 MHz image, although in the latter data the emission does not quite disappear down to the noise level, since the synthesized beam of 25 arcmin is too large to fully resolve this feature. The difference in the large-scale morphologies between the northern and southern lobes is quite distinct, with the northern lobe characterized by an abrupt change in position angle producing the northern hook feature and the southern lobe having a much smoother variation
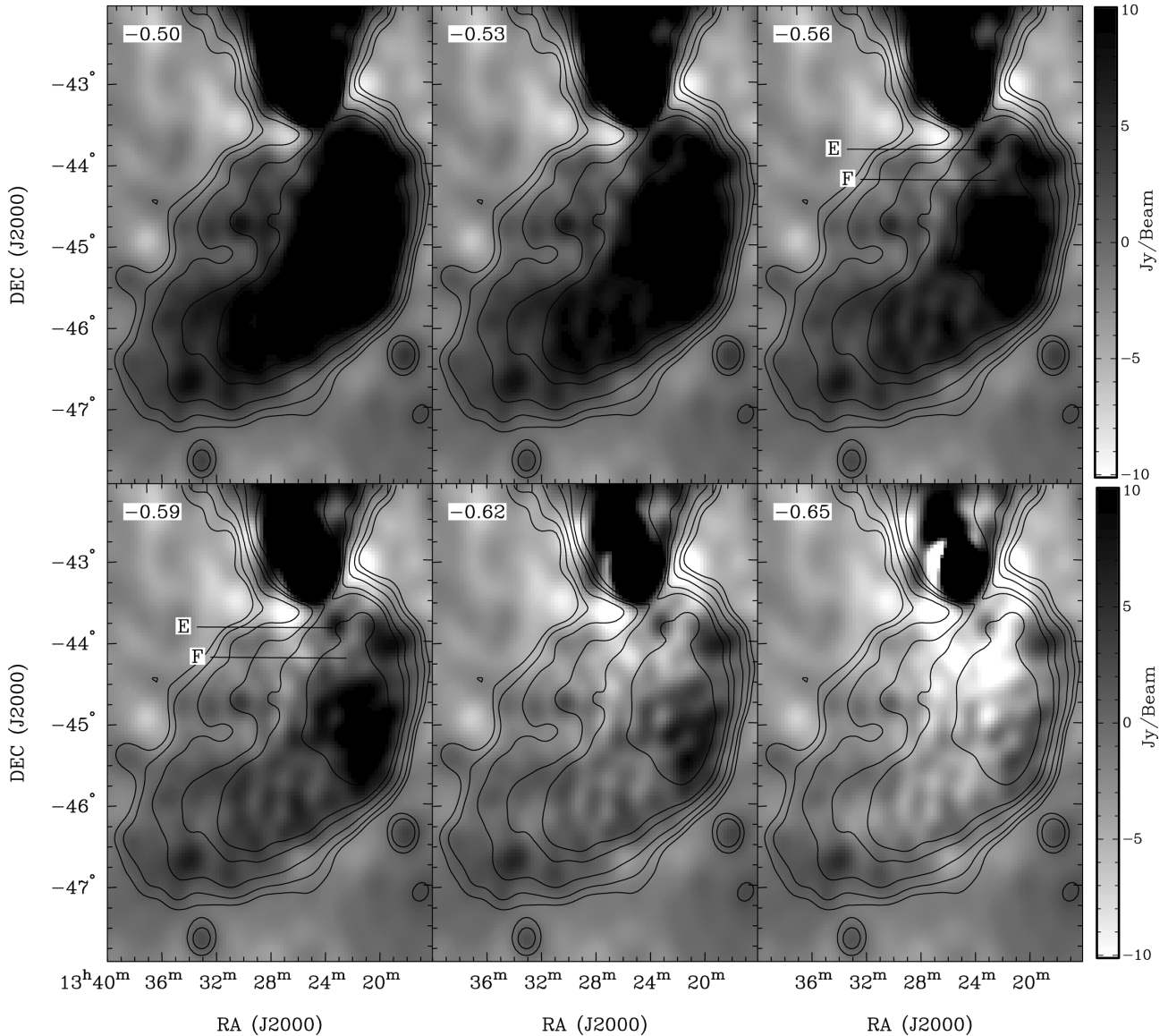
Figure 10. As for Fig. 9, but for the southern lobe with contours from the 118 MHz image at 2.5, 5, 10, 20, 28.3 and 56.5 Jy beam^{-1}. The feature labelled E has a significantly steeper spectral index than that labelled F.

in orientation. These large-scale features mirror the morphology of the inner lobes as imaged at high spatial resolution with the Very Large Array (Schreier et al. 1981; Clarke et al. 1992). In the north, a sudden change in position angle of the radio emission is also seen at an intermediate scale in the NML, as imaged in detail by Morganti et al. (1999; see e.g. their fig. 4). An explanation for the existence of the intermediate scale NML and the fact that it mirrors the shape of the inner lobes was proposed by Morganti et al. (1999), who suggested that the central engine has undergone multiple outbursts of activity. In this scenario, the inner lobes are due to the most recent outburst and the middle and outer lobes are relics of past activity. They suggest that the distinctive shape of the NML and its associated large-scale jet could be due to a similar type of interaction with the surrounding environment that produces the class of radio galaxies known as wide-angled tailed (WAT) radio galaxies. Norman et al. (1988) used numerical simulations of jets disrupted by shocks in the ambient medium to reproduce the structure of WATs and the inner northern jet of Cen A. If the inner lobes are the result of the current

outburst of activity from the core and the NML is the result of a previous outburst, then the outer northern lobe with its hook-like structure seen at frequencies below 5 GHz is probably the result of similar previous outbursts of AGN activity. In order to build up such large, energetic structures as the giant outer lobes, many outbursts similar to the current inner lobe activity are likely to have been required.

Clear evidence of multiple, separate outbursts of activity in radio galaxies is seen in the class of radio galaxies known as 'double-double' radio galaxies (see e.g., Schoenmakers et al. 2000; Jamrozy et al. 2009). However, these are characterized by edge-brightened lobes like those seen in FRII galaxies. Jamrozy et al. (2009) single out several other radio galaxies that show evidence of multiple outbursts of activity including 3CR310 (Leahy, Pooley & Riley 1986), the WAT galaxy in the cluster A 2372 (Giacintucci et al. 2007), Hercules A (Her A, Gizani & Leahy 2003) and also Cen A. Spectral-index maps of the WAT galaxy in A 2372 and Her A show similar features to our spectral-tomography results, where
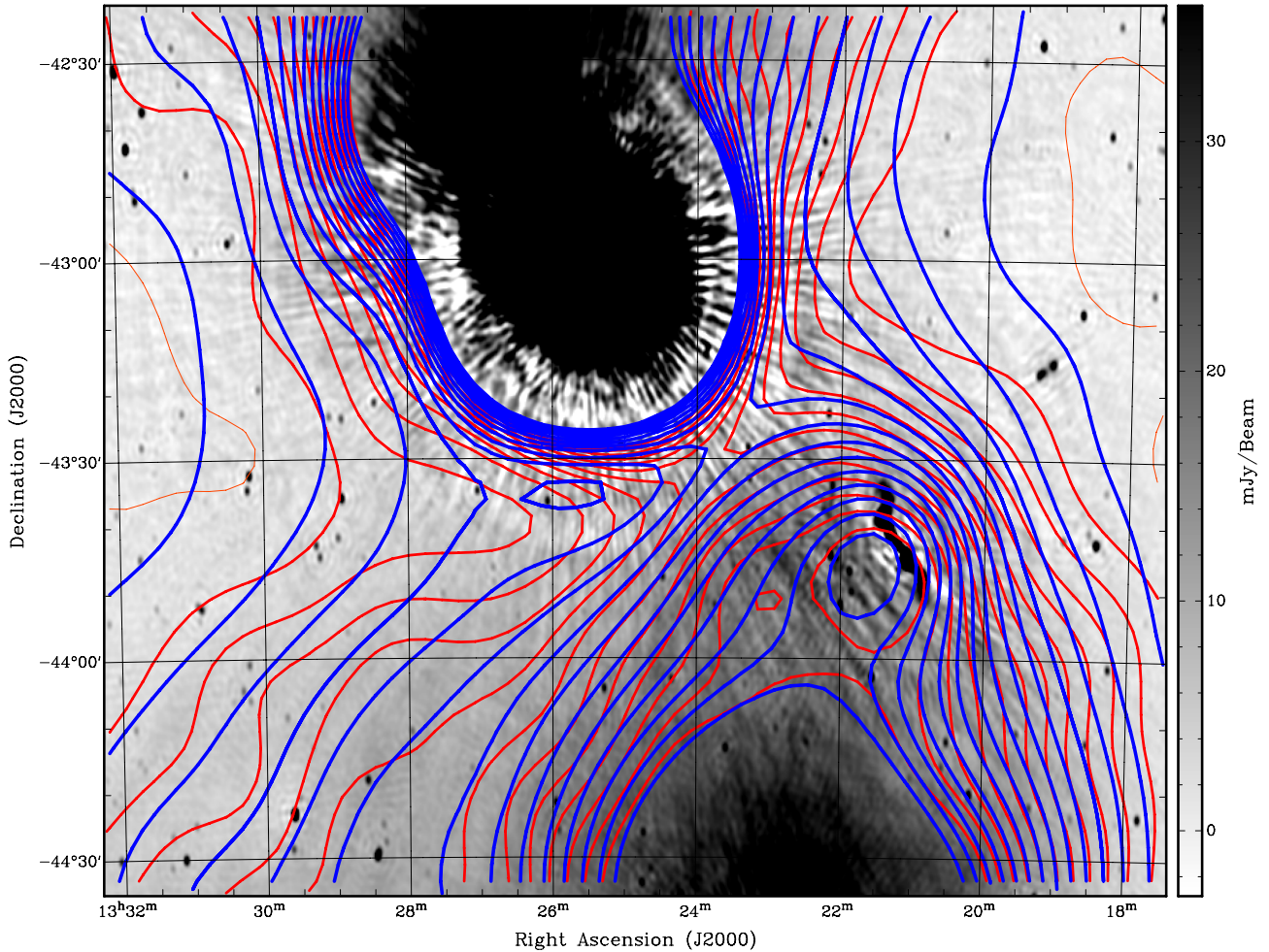
Figure 11. High-resolution 1.4 GHz Parkes+ATCA map (Feain et al. 2011) in grey-scale, overlaid with the 1.4 GHz Parkes contours (O'Sullivan et al. 2013) in blue and the MWA 118 MHz contours in red. Positive 118 MHz MWA contours are from 3 Jy beam^{-1} incrementing in steps of 5 Jy beam^{-1} and 1.4 GHz Parkes contours are from 1 Jy beam^{-1} incrementing in steps of 1 Jy beam^{-1}. There is one negative contour visible, which is the -3 Jy beam^{-1} level of the 118 MHz map, shown as a thinner, lighter red line. There is a peak at 13^h23^m, $-43°51'$ in the 118 MHz map that is not visible in the 1.4 GHz images and does not coincide with any background sources visible at 1.4 GHz. The bright background source MRC 1318−434B, at $13^h21^m18^s$, $-43°41'15''$, extends approximately 20 arcmin and is coincidentally aligned with the position angle of the inner lobes of Cen A.

the spectral index changes with distance from the core, showing alternating regions of flatter and steeper spectral index indicating different spectral ages across the lobes. In our spectral-tomography results for the northern lobe of Cen A (Fig. 9), we show that the spectral index steepens along the extended structure associated with NML from point D to point C, indicating an older population of particles further from the core. The spectrum then flattens again at point A, which could be due to reacceleration of particles in this region, caused by interaction with newer, more energetic particles from the outburst that created the NML. The new material catches up to the old lobes as it has a less dense medium to travel through, as shown in numerical simulations by Clarke & Burns (1991). Finally, the spectrum steepens again at the end of the northern hook (point B in Fig. 9); this could indicate an older population of particles that has not experienced reacceleration, possibly because the central engine has precessed and the subsequent outbursts are not directed towards this region. The spectral variations we observe in Cen A, however, are relatively subtle. In most cases $\Delta\alpha_{118}^{1400} < 0.1$, while in Her A $\Delta\alpha_{1300}^{4800} \approx 0.8$ between the bridge and the jet and ring features (Gizani & Leahy 2003). While some of the difference in magnitude

of the spectral variation can be attributed to the lower frequency of the Cen A spectral-index measurement, it is possible that variations in the magnetic field strength or the initial jet spectrum may be enough to cause such variations without the need for reacceleration.

The structure of Cen A is complicated by the bending of the lobes, which is probably due to both the interaction with the ambient medium (Morganti et al. 1999), at least for the northern lobe, and the precession or reorientation of the central engine over time (Haynes et al. 1983). The radio morphology of Cen A at small, intermediate and large scales supports the multiple-outburst scenario described above, where there appear to have been three epochs of activity that formed the inner, middle and outer lobes, respectively. However, the detailed timing of these outbursts of activity is difficult to determine and remains unclear. Hardcastle et al. (2009) calculate spectral ages of $\sim$30 Myr for the outer lobes of Cen A and Haynes et al. (1983) calculate a precession rate for the central engine of 1×10^{-5} deg yr^{-1} from the stellar ages of observed B supergiants near the NML (Osmer 1978). This implies that over the time of formation of the outer lobes, there were several precessional periods of the central engine and also time for several outbursts of activity

on similar scales to that which formed the inner lobes, which have an estimated spectral age of $\sim$5 Myr (Burns, Feigelson & Schreier 1983). In a separate analysis, Wykes et al. (2013) estimate much greater ages for the giant lobes of 440 to 645 Myr and 560 Myr (for both lobes) based on dynamical and buoyancy arguments, respectively, which would allow time for many more outbursts of activity and precessional periods. Wykes et al. (2013), however, recognize that their age estimates differ from ages derived by radio spectral-index information by a large amount and we note that the arguments they base their calculations on are known to overestimate lobe ages in radio galaxies as detailed in McNamara & Nulsen (2007).

A problem with the multiple-outburst scenario is the apparent non-existence of a southern counterpart to the NML. Our 118 MHz map and spectral-tomography results do, however, indicate the existence of a steeper spectrum component along the southern lobe (see Figs 10 and 11) at a location that is at approximately the correct position angle to be associated with the same period of activity as the NML. Whether this is evidence for the existence of a faint, steep spectrum feature associated with a 'southern middle lobe' will be investigated through future observations with the full 128-tile MWA, which will provide higher angular resolution and increased sensitivity to such diffuse radio structures.

5.2 Comparison to gamma-ray data

Yang et al. (2012) model the SEDs of the northern and southern lobes of Cen A using gamma-ray observations from *Fermi*-LAT and radio data from ground-based telescopes (see Hardcastle et al. 2009) and WMAP (Hinshaw et al. 2009; Komatsu et al. 2011). They present SEDs from inverse-Compton models, which predict the flux density of the radio emission at low frequencies, integrated over the entire gamma-ray emitting region of the lobes. Figs 8 and 9 of Yang et al. (2012) show SEDs for two values of the model age of the outer lobes, t, selected based on the approximate lower limit of the lobe ages of 10^7 years, set by dynamical arguments and the modelling of Hardcastle et al. (2009), and an upper limit of 10^8 years, supported by the GeV data in the Yang et al. (2012) paper itself. We determine the predicted two-point spectral index between 118 MHz and 1.4 GHz for both of the Yang et al. (2012) models. For a lobe age of 10 Myr the predicted spectral index in both the northern and southern lobes is approximately -0.62 and for a lobe age of 80 Myr the predicted spectral index in both lobes is -0.57. Our values for the average spectral indices of the lobes as derived from the T-T plots (Fig. 8) of $\alpha_{1,2} = -0.66 \pm 0.01(\text{stat})^{+0.10_{\text{sys}}}_{-0.08_{\text{sys}}}$ in the northern lobe and $\alpha_4 = -0.63 \pm 0.01(\text{stat})^{+0.10_{\text{sys}}}_{-0.08_{\text{sys}}}$ and $\alpha_5 = -0.65 \pm 0.01(\text{stat})^{+0.10_{\text{sys}}}_{-0.08_{\text{sys}}}$ in the southern lobe, are consistent with both of these predictions. The difference between the predicted spectral indices is too small for us to distinguish between the lobe ages from our measured spectral indices and in any case the modelling of Yang et al. (2012) can only be considered a first-order approximation to the true physical conditions. Assumptions such as a single age and spectral index for the lobes, a constant magnetic field and constant particle densities have been shown to be untrue (see e.g. Junkes et al. 1993; Feain et al. 2011, this work) therefore more detailed theoretical models are needed to take full advantage of current and future observational data.

6 CONCLUSION

We have imaged the entirety of Cen A and a large surrounding field at 118 MHz with the MWA 32T. The wide field of view and good uv-coverage of the MWA 32T allow us to map the giant lobes at a reasonable angular resolution and to reconstruct their large-scale structure. We have investigated the spatially resolved spectral properties of the giant lobes by comparing the MWA map at 118 MHz to Parkes data at 1.4 GHz. Through the use of T-T plots and spectral tomography, we find that the spectral index of the lobes between 118 MHz and 1.4 GHz has a spatially averaged value consistent with measurements at other frequencies, but that there is a complex spatial distribution of spectral index across the lobes. The morphology and spectral-index distribution of the lobes support a scenario of multiple outbursts from a precessing central engine, and we find tentative evidence for the existence of a faint, steep spectrum southern counterpart to the NML. We find that our results also agree well with the inverse-Compton modelling of gamma-ray and radio data. Future observations with the complete 128-tile MWA will provide a more detailed picture of the low-frequency properties of Cen A, which can be used to constrain more complex theoretical models.

REFERENCES

Abdo A. A. et al., 2010, Sci, 328, 725
Alvarez H., Aparici J., May J., Olmos F., 1997, A&AS, 124, 315
Alvarez H., Aparici J., May J., Reich P., 2000, A&A, 355, 863
Atwood W. B. et al., 2009, ApJ, 697, 1071
Baars J. W. M., Genzel R., Pauliny-Toth I. I. K., Witzel A., 1977, A&A, 61, 99
Begelman M. C., Blandford R. D., Rees M. J., 1984, Rev. Mod. Phys., 56, 255
Bernardi G. et al., 2009, A&A, 500, 965
Bernardi G. et al., 2013, ApJ, 771, 105
Boggs P. T., Rogers J. E., 1990, Contemp. Math., 112, 186

Bolton J. G., 1948, Nat, 162, 141

Bowman J. D. et al., 2013, Publ. Astron. Soc. Aust., 30, 31

Burns J. O., 1986, Can. J. Phys., 64, 373

Burns J. O., Feigelson E. D., Schreier E. J., 1983, ApJ, 273, 128

Clarke D. A., Burns J. O., 1991, ApJ, 369, 308

Clarke D. A., Burns J. O., Norman M. L., 1992, ApJ, 395, 444

Combi J. A., Romero G. E., 1997, A&AS, 121, 11

Cooper B. F. C., Price R. M., Cole D. J., 1965, Aust. J. Phys., 18, 589

Cornwell T. J., Golap K., Bhatnagar S., 2008, IEEE J. Sel. Top. Signal Process., 2, 647

de Oliveira-Costa A., Tegmark M., Gaensler B. M., Jonas J., Landecker T. L., Reich P., 2008, MNRAS, 388, 247

DeLaney T., Koralesky B., Rudnick L., Dickel J. R., 2002, ApJ, 580, 914

Ellis G. R. A., Hamilton P. A, 1966, ApJ, 143, 227

Fanaroff B. L., Riley J. M., 1974, MNRAS, 167, 31

Feain I. J. et al., 2011, ApJ, 740, 17

Furlanetto S. R. et al., 2006, Phys. Rep., 433, 4

Gaensler B. M., Wallace B. J., 2003, ApJ, 594, 326

Giacintucci S., Venturi T., Murgia M., Dallacasa D., Athreya R., Bardelli S., Mazzotta P., Saikia D. J., 2007, A&A, 476, 99

Gizani N. A. B., Leahy J. P., 2003, MNRAS, 342, 399

Gopal-Krishna, Saripalli L., 1984, A&A, 141, 61

Gopal-Krishna, Wiita P. J., 2010, New Astron., 15, 96

Hamilton P. A., Haynes R. F., 1968, Aust. J. Phys., 21, 895

Hardcastle M. J., Cheung C. C., Feain I. J., Stawarz Ł., 2009, MNRAS, 393, 1041

Harris G. L. H., Rejkuba M., Harris W. E., 2010, Publ. Astron. Soc. Aust., 27, 457

Haslam C. G., Salter C. J., Stoffel H., Wilson W. E., 1982, A&AS, 47, 1

Haynes R. F., Cannon R. D., Ekers R. D., 1983, Publ. Astron. Soc. Aust., 5, 241

Hinshaw G. et al., 2009, ApJS, 180, 225

Israel F. P., 1998, A&AR, 8, 237

Jacobs D. C., Bowman J., Aguirre J. E., 2013, ApJ, 769, 5

Jamrozy M., Konar C., Saikia D. J., Machalski J., 2009, in Saikia D. J., Green D. A., Gupta Y., Venturi T., eds, ASP Conf. Ser. Vol. 36, The Low-Frequency Radio Universe. Astron. Soc. Pac., San Francisco, p. 137

Junkes N., Haynes R. F., Harnett J. I., Jauncey D. L., 1993, A&A, 269, 29

Katz-Stone D. M., Rudnick L., 1997, ApJ, 488, 146

Komatsu E. et al., 2011, ApJS, 192, 18

Large M. I., Mills B. Y., Little A. G., Crawford D. F., Sutton J. M, 1981, MNRAS, 194, 693

Leahy J. P., Pooley G. G., Riley J. M., 1986, MNRAS, 222, 753

Lonsdale C. J. et al., 2009, Proc. IEEE, 97, 1497

Ma C. et al., 1998, AJ, 116, 516

Malin D. F., Quinn P. J., Graham J. A., 1983, ApJ, 272, 5

Mauch T., Murphy T., Buttery H. J., Curran J., Hunstead R. W., Piestrzynski B., Robertson J. G., Sadler E. M., 2003, MNRAS, 342, 1117

McNamara B. R., Nulsen P. E. J., 2007, ARA&A, 45, 117

Morales M. F., Wyithe J. S. B., 2010, ARA&A, 48, 127

Morganti R., Killeen N. E. B., Ekers R. D., Oosterloo T. A., 1999, MNRAS, 307, 750

Norman M. L., Burns J. O., Sulkanen M. E., 1988, Nat, 335, 146

O'Sullivan S. P. et al., 2013, ApJ, 764, 162

Offringa A. R., de Bruyn A. G., Biehl M., Zaroubi S., Bernardi G., Pandey V. N., 2010, MNRAS, 405, 155

Offringa A. R., van de Gronde J. J., Roerdink J. B. T. M., 2012, A&A, 539, 95

Osmer P. S., 1978, ApJ, 226, 79

Parsons A. R. et al., 2010, AJ, 139, 1468

Pritchard J. R., Loeb A., 2012, Rep. Prog. in Phys., 75, 086901

Reynolds J. E., 1994, ATNF Tech. Memo, 39.3/040: A Revised Flux Scale for the AT Compact Array. Australia Telescope National Facility, Epping

Saxton C. J., Sutherland R. S., Bicknell G. V., 2001, ApJ, 563, 103

Schilizzi R. T., McAdam W. B., 1975, Mem. R. Astron. Soc., 79, 1

Schiminovich D., van Gorkom J. H., van der Hulst J. M., Kasow S., 1994, ApJ, 423, L101

Schoenmakers A. P., de Bruyn A. G., Röttgering H. J. A., van der Laan H., Kaiser C. R., 2000, MNRAS, 315, 371

Schreier E. J., Burns J. O., Feigelson E. D., 1981, ApJ, 251, 523

Shain C. A., 1959, in Ronald N. B., ed., Proc. IAU Symp. 9, Paris Symposium on Radio Astronomy. Stanford Univ. Press, Stanford, p. 328

Sheridan K. V., 1958, Aust. J. Phys., 11, 400

Slee O. B., 1977, Aust. J. Phys. Astrophys. Suppl., 43, 1

Slee O. B., 1995, Aust. J. Phys., 48, 143

Stefan I. I. et al., 2013, MNRAS, 432, 1285

Stickel M., van der Hulst J. M., van Gorkom J. H., Schiminovich D., Carilli C. L., 2004, A&A, 415, 95

Subrahmanyan R., Saripalli L., Hunstead R. W., 1996, MNRAS, 279, 257

Tingay S. J. et al., 2013, Publ. Astron. Soc. Aust., 30, 7

Turtle A. J., Pugh J. F., Kenderdine S., Pauliny-Toth I. I. K., 1962, MNRAS, 124, 297

van Haarlem M. P. et al., 2013, A&A, 556, A2

Williams C. L. et al., 2012, ApJ, 755, 47

Wykes S. et al., 2013, A&A, preprint (arXiv:1305.2761)

Yang R. Z., Sahakyan N., de Ona Wilhelmi E., Aharonian F., Rieger F, 2012, A&A, 542, 19

This paper has been typeset from a TEX/LATEX file prepared by the author.